AGU PUBLICATIONS

Journal of Advances in Modeling Earth Systems

RESEARCH ARTICLE
10.1002/2016MS000685

Dynamical downscaling of tropical cyclones from CCSM4 simulations of the Last Glacial Maximum

Jinwoong Yoo[1], Joseph Galewsky[1], Suzana J. Camargo[2], Robert Korty[3], and Ryan Zamora[3]

[1]Department of Earth and Planetary Sciences, University of New Mexico, Albuquerque, New Mexico, USA, [2]Lamont-Doherty Earth Observatory, Columbia University, New York, New York, USA, [3]Department of Atmospheric Sciences, Texas A&M University, College Station, Texas, USA

Key Points:
- Downscaled LGM TC climatology does not differ from the twentieth century
- Downscaled environmental factors are consistent with simulated TCs
- Changes in TC genesis density between LGM and 20C are represented by the ventilation index

Correspondence to:
J. Galewsky,
galewsky@unm.edu

Citation:
Yoo, J., J. Galewsky, S. J. Camargo, R. Korty, and R. Zamora (2016), Dynamical downscaling of tropical cyclones from CCSM4 simulations of the Last Glacial Maximum, *J. Adv. Model. Earth Syst.*, *8*, 1229–1247, doi:10.1002/2016MS000685.

Received 1 APR 2016
Accepted 12 JUL 2016
Accepted article online 14 JUL 2016
Published online 11 AUG 2016

Abstract Dynamical downscaling of simulations of the Last Glacial Maximum (LGM) and late twentieth century (20C) were conducted using the Weather Research and Forecasting (WRF) model with the aim of (1) understanding how the downscaled kinematic and thermodynamic variables influence simulated tropical cyclone (TC) activity over the western North Pacific during the LGM and the 20C periods and (2) to test the relevance of TC genesis factors for the colder LGM climate. The results show that, despite the lower temperatures during the LGM, the downscaled TC climatology over the western North Pacific in the LGM simulation does not differ significantly from that in the 20C simulation. Among the TC environmental factors, the TC potential intensity, mid-tropospheric entropy deficit, and vertical wind shear during the LGM were consistent with previous analyses of TC genesis factors in LGM global climate model simulations. Changes in TC genesis density between the LGM and the 20C simulations seem to be well represented by the ventilation index, a nondimensional measure of the combined effects of vertical wind shear, and thermodynamic properties, suggesting the potential applicability of those factors for TC activity evaluation during the LGM and possibly other climates.

1. Introduction

During the past decade, there has been a vigorous interest in the question of how tropical cyclones (TCs) respond to climate change. *Emanuel* [2005] and *Webster et al*. [2005] related increases in intense storms to concurrent increases in sea surface temperatures, but questions regarding the accuracy and completeness of the historical TC record persist [e.g., *Landsea et al*., 2006; *Klotzbach and Landsea*, 2015], and reliable global data are limited only to the recent decades of the satellite era. Efforts to understand how storms may respond to projections of climate changes over the next century have largely focused on analysis of model simulations; these include analysis of large-scale environmental factors known to favor genesis and intensification [e.g., *Camargo et al*., 2007a, 2007b, 2014], analysis of explicitly resolved storms simulated directly in global climate models [e.g., *Camargo*, 2013; *Camargo and Wing*, 2016], and several downscaling techniques to simulate storms in higher-resolution models better suited to resolving storm structure and intensity [e.g., *Emanuel*, 2013; *Knutson et al*., 2015].

Under global warming scenarios, these studies found that the intensity of the most intense TCs is likely to increase by the end of the 21st century, while their global frequency is most likely reduced [*Knutson et al*., 2010; *Walsh et al*., 2016]. These projections are obtained using high-resolution global climate models [e.g., *Murakami et al*., 2012; *Zhao and Held*, 2012], high-resolution idealized experiments [*Rappin et al*., 2010; *Merlis et al*., 2016], as well as using dynamical downscaling using regional climate models [*Knutson et al*., 2008; *Bender et al*., 2010]. For instance, *Knutson et al*. [2015] considered storms produced by a global model, but then used a higher-resolution model in order to simulate the most intense storms. The increase in the occurrence of the most intense storms under global warming is consistent with increases in potential intensity [e.g., *Emanuel*, 1987], while the decrease in the number of storms simulated with warming may be sensitive to the survival of weak systems [e.g., *Emanuel et al*., 2010]. Furthermore, *Emanuel* [2013] applied a downscaling method that synthetically generates tracks and found a statistically significant increase in the number and intensity of storms over the 21st century, in contrast with results from studies that explicitly simulate and track warm-core vortices. We believe it worthwhile to apply downscaling techniques to

simulations under very different climate scenarios. At a minimum, it may be useful to learn how the models tasked with projecting future scenarios behave under a wider range of climate forcing.

We used the Weather Research and Forecasting model (WRF) to downscale output of a global model's simulation of the Last Glacial Maximum (LGM) conditions of 21,000 years ago (21 ka) and late twentieth century (20C) with the aim of simulating the TC climatology in the western North Pacific basin. We believe that these tests provide an interesting contrast to the studies of future warming projections by examining behavior in a radically different and colder climate. In particular, it is of interest to compare the changes in TC activity during the LGM with other cooling scenarios, such as the uniform cooling of 4 K investigated by *Sugi et al*. [2015]. They obtained a significant increase in global TC frequency in a high-resolution global climate model under these colder conditions.

Moreover, there is significant interest in the field of paleotempestology to understand the conditions that affected the prehistoric record of TCs revealed by geologic proxies. While some widely used methods [e.g., *Liu and Fearn*, 1993; *Donnelly and Woodruff*, 2007; *Frappier et al*., 2007] provide data only for the most recent millennia (for which sedimentary records of overwash from barrier islands are available), nascent techniques using deep-sea cores recovered from sloping banks near the Florida current show the potential to uncover records back to earlier periods [*Toomey et al*., 2013]. Furthermore, some understanding (even qualitative) of the behavior of TCs during glacial periods would be useful to geologists, who have shown that tropical storms affected the geological evolution of islands in the western Pacific [*Galewsky et al*., 2006; *Lin et al*., 2008; *Hayakawa and Takashi*, 2009; *Woodruff et al*., 2009; *Stark et al*., 2010].

This is not the first attempt to simulate tropical cyclones in LGM conditions. *Hobgood and Cerveny* [1988] applied a four-layer model [*Anthes*, 1972; *Hobgood*, 1986] to simulate the development of a TC with two sets of initial conditions: one with vertical temperature and moisture profiles common to the modern-day tropics, and a second with those taken from the more stable profiles produced in an ice-age simulation by the Goddard Institute for Space Studies (GISS) climate model [*Hansen et al*., 1984]. Their model developed storms of moderate intensity in both climates, but the early GISS simulation from which the initial conditions for the ice-age were taken suffered from a large radiation imbalance that arose, in part, from marrying the estimates of LGM sea surface temperatures (SSTs) that were in wide use at the time [*CLIMAP Project Members*, 1976] with specific levels of carbon dioxide. We feel a fresh look at the issue with contemporary models is worthwhile.

We focus here on the western North Pacific basin, which produces more TCs than any other region in the world today [e.g., *Chan*, 2015]. Despite the universally colder conditions at LGM, *Korty et al*. [2012a] found that many simulations from the Paleoclimate Modelling Intercomparison Project Phase 2 (PMIP2) featured environmental conditions in the western North Pacific as favorable as they are in the modern climate, at least in portions of this basin. *Koh and Brierley* [2015] confirmed those results in the more recent suite of LGM simulations included in Phase 3 (PMIP3). However, there is important model-to-model variability in the environmental conditions at LGM, so results generated by downscaling from other global models might depart from specific details presented here. While future studies will focus on the Atlantic and eastern North Pacific, we chose the western North Pacific for this study because of the particular impact of tropical cyclones on Earth surface processes on the mountainous islands in that region during the Quaternary [e.g., *Galewsky et al*., 2006; *Stark et al*., 2010], and the hope that downscaling of tropical cyclones may provide improved constraints for models of erosion and sediment transport around the western North Pacific.

This paper is organized as follows. In section 2, we briefly describe the WRF model physics used for the dynamically downscaled simulations. Section 3 compares the large-scale climatology of the dynamical downscaled experiments to that of the global model. Section 4 presents the TC activity during the LGM and modern-day control cases. We compare the TC climatology with the environmental factors known to influence TC activity in section 5, and a summary and conclusions are presented in section 6.

2. Data and Methods

Ten year long downscaling of CCSM4 (Community Climate System Model version 4) twentieth century (1990–1999) and LGM (model simulation years 1871–1880 used below reflects the model's internal reference calendar for LGM years) runs [*Brady et al*., 2013] from phase five of the Coupled Model

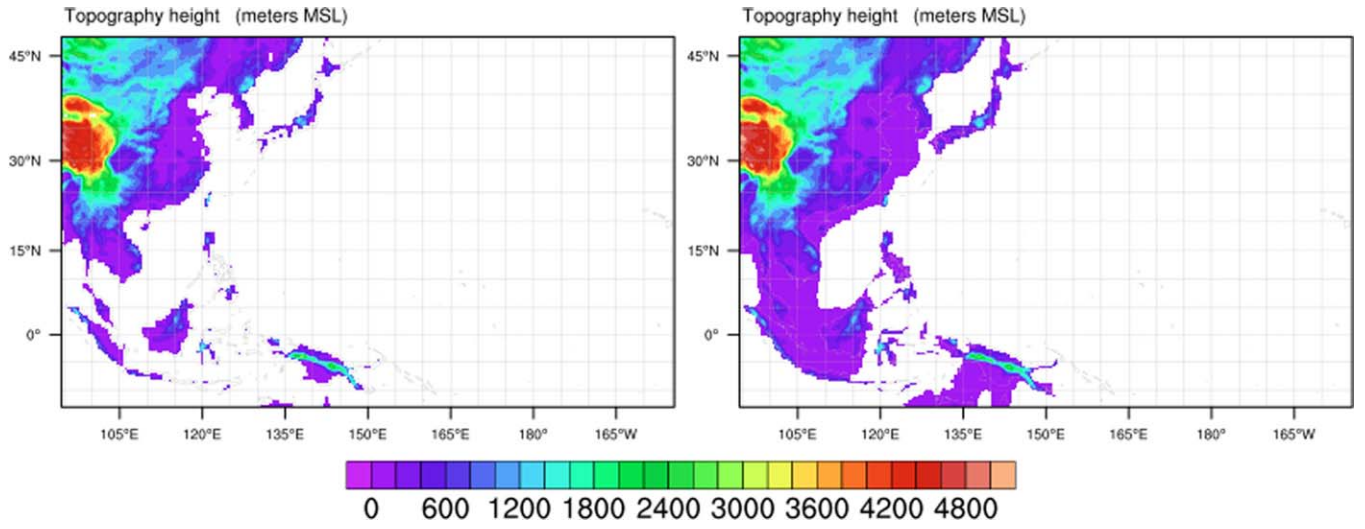

Figure 1. WRF model domains with topography for the (left) 20C and (right) LGM periods.

Intercomparison Project (CMIP5) and Paleoclimate Modelling Intercomparison Project Phase 3 (PMIP3) was computed using the Advanced Research version of the Weather Research and Forecasting model (WRF-ARW, called here WRF) version 3.1.5 [*Skamarock et al*., 2005], which is capable of long-term climate simulations [e.g., *Done et al*., 2006; *Yu et al*., 2014]. The CCSM4 output used as initial and boundary conditions for the WRF LGM simulations was obtained from 1000 years long LGM simulations that were run to a state of close to statistical equilibrium [*Brady et al*., 2013] and has a horizontal grid spacing of ∼0.94° latitude by 1.25° longitude.

The WRF model is capable of simulating many aspects of the dynamics and physics of TC lifecycles [e.g., *Kieu and Zhang*, 2008], reproducing observed TC structure and intensities when using grid spacings on the order of a few kilometers [*Davis et al*., 2008]. For regional TC climate simulation, domain size and grid spacing play important roles [*Vannitsem and Chome*, 2005; *Kumar et al*., 2011; *Done et al*., 2015]. In particular, high spatial resolution is needed to simulate the full spectrum of observed TC intensities up to Category 5 in the Saffir-Simpson scale, and model grid spacing should be as small as in operational forecasting models (∼4 km) [*Bender et al*., 2010; *Done et al*., 2015; *Knutson et al*., 2015]. Only recently, global climate models with a horizontal grid with resolution above ∼18 km started to be able to simulate major hurricanes (Categories 3–5) with maximum winds greater than 50 m s^{-1} [*Murakami et al*., 2015], but even those that cannot simulate the most intense storms have been useful to study other aspects of the TC climatology such as their frequency, genesis, and intensity changes in weaker systems [*Knutson et al*., 2008]. For more discussion on practical issues with dynamical downscaling of TCs using the WRF model, see *Done et al*. [2015, and references therein].

For the simulations presented here, we balanced the benefits of horizontal high resolution against the computational constraints of long-term climate simulations and configured the WRF model domain with a grid spacing of 36 km; this features 171 latitude points and 282 longitude points over the western North Pacific domain for the LGM and the 20C periods. At this resolution, our emphasis is primarily on changes to genesis and tracks, but we also report difference in the limited portion of the intensity distribution we are able to resolve. The WRF model domain is shown in Figure 1 and spans latitudes 13.066°S–47.435°N and longitudes 93.75°E–206.25°E. Following *Brady et al*. [2013], the LGM coastlines reflect a sea level that was 120 m lower than the modern period, with WRF vegetation parameters for the exposed land surface drawn from CLIMAP LGM vegetation [*CLIMAP Project Members*, 1976] mapped onto the USGS land use categorization used in the WRF model. Except for modifications to the short-wave and long-wave radiation schemes for the LGM simulation and the modifications to account for the exposed coastal regions, the model physics used for the LGM and the 20C simulations are identical. The Community Atmospheric Model (CAM) radiation scheme for the LGM simulation was modified to be consistent with the LGM radiation of the PMIP3/CMIP5 experiment (Table 1), and accounts for the different orbital parameters and greenhouse gas forcing during the LGM

Table 1. Boundary Conditions, Trace Gases, and Earth's Orbital Parameters

	Ice Sheets	Topography Coastlines	CO_2 (ppmv)	CH_4 (ppbv)	NO_2 (ppbv)	Eccentricity	Obliquity (°)	Angular presession (°)
20C (0 ka)	20C	20C	280	760	270	0.0167724	23.446	102.04
LGM (21 ka)	ICE-5G	ICE-5G	185	350	200	0.018994	22.949	114.42

[*Braconnot et al.*, 2007]. The simulations used the WRF Single-Moment 6-class scheme for microphysics; MM5 (Pennsylvania State University—National Center for Atmospheric Research Mesoscale Model version 5) similarity scheme based on Monin-Obukhov with Carslon-Boland viscous sublayer for the surface layer option; the Noah Land Surface Model (LSM); the Yonsei University planetary boundary layer (PBL) scheme; and the Kain-Fritsch convective parameterization. A terrain following nonhydrostatic pressure vertical coordinate is used with 51 levels, and the model top was set at 10 hPa. Model SST and skin temperature were updated every time step.

3. Dynamical Downscaling Results

The WRF simulations capture the first-order climate properties of the LGM and the 20C climates inherited from the CCSM4 simulations. Comparisons of 2 m air temperature (T2) between the WRF and CCSM4 simulations (Figure 2) during the LGM (left column) and 20C (center column) show that the WRF model produced a negative bias: the domain average bias (root-mean-square error, RMSE) was −1.4 (1.78)°C for the LGM and −0.95 (1.64)°C for 20C. The negative bias is most pronounced over the midlatitude coastal region and downwind over adjacent ocean. Latitudinal and monthly distributions of 10 year averages of T2 from the WRF and CCSM4 simulations both for the LGM and 20C periods (Figure 3) suggest that the WRF simulations generally reproduced the temporal variance of T2 in the CCSM4. Compared to the CCSM4 simulations, the WRF simulations underestimated T2 during the summer season and overestimated T2 during the fall and winter seasons over the region poleward of 15°N, while they slightly overpredicted T2 over the low-latitude tropical region (13°S–10°N) in the western North Pacific from March to December. The underestimation of T2 was more pronounced in the 20C simulation than in the LGM simulation. These deviations from the CCSM4 results may be attributed in part to the model physics [*Lo et al.*, 2008] and to the higher spatial resolution in the WRF simulations. Model bias can also be potentially introduced by calculating the zonal averages and regridding the high-resolution WRF results to match the coarse CCSM4 grid.

The average relative humidity at 2 m (RH2; Figure 4) over the 10 simulated years of LGM climate was 86% in WRF and was 79% in CCSM4. The 10 year average of RH2 for the 20C simulation was also higher in WRF than CCSM4: 88% in WRF and 80% in CCSM4. Compared to the CCSM4 simulations, the WRF simulations have a wet bias over the ocean and a dry bias over the land both in the LGM and the 20C simulations. Higher RH2 values over the ocean can affect the potential intensity of TCs by reducing the strength of thermodynamic disequilibrium on which surface enthalpy fluxes depend [*Emanuel*, 1987].

The WRF simulations reproduced the drier continental surface during the LGM compared to that of the 20C climate, while RH2 over the open ocean does not differ much between the LGM and the 20C both for the WRF and the CCSM4 simulations. While it is possible that differences in convective or microphysical parameterizations or in the Noah land surface model in WRF are responsible for those spatial differences in RH2, further diagnostics for those differences are beyond the scope of this study.

4. TCs Detected in the Downscaled Simulations

Some fields from a typical WRF-simulated TC are shown in Figure 5. The 36 km grid spacing reproduces the general characteristics of TC structures relatively well within the plots of sea level pressure (hPa), precipitable water (PW; mm), absolute vorticity (10^{-5} s^{-1}), relative humidity (%), and wind speed (kts) at 850 hPa. Although the eyewall structure is not clear in the 36 km resolution simulation, the eyewall location can be identified by the maximum in PW (Figure 5b). The PW plot of this storm also shows dry air entrainment into the center of storm from the west (Figure 5b). The rainband structure around the center of the storm can be seen in the plots of absolute vorticity and relative humidity (Figures 5c and 5d). These structural features represent a clear improvement of the regional-scale model over fields in the coarser resolution GCM (not

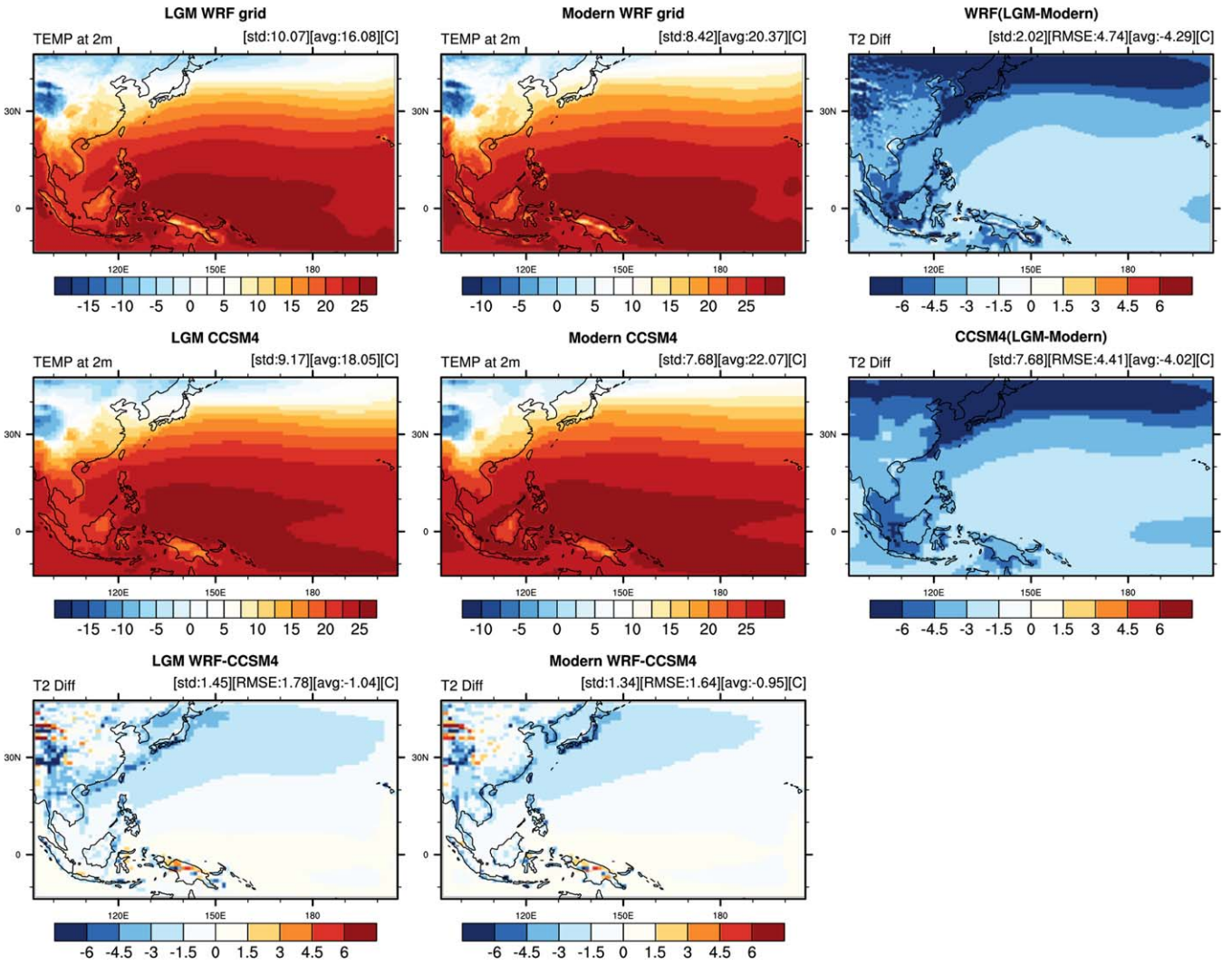

Figure 2. Comparison of 10 year averages of 2 m air temperature from WRF and CCSM4 simulations for LGM and late 20C periods. Plots on left (center) column show the comparison between the WRF and CCSM4 during the LGM (late 20C) period. Two plots at the bottom represent the WRF model bias from CCSM4 results for the LGM and late 20C simulation periods. Two plots on the right column show the 2 m air temperature differences between the LGM and late 20C simulation periods from the (top) WRF and (bottom) CCSM4 simulations. Domain averages and standard deviations are represented at the top of each plot. RMSE is included for the T2 difference plots.

shown). Our WRF simulations resolve storms with peak intensities up to ~55 m/s, while the majority of those explicitly resolved in the GCM feature surface winds 15–25 m/s.

For this study, TC tracks were obtained using two tracking algorithms: the first developed by *Camargo and Zebiak* [2002, CZ02, hereafter] and the second by Kevin Hodges (TRACK version 4.1.6) [*Hodges*, 1994, 1995, 1996, H96, hereafter] both for the LGM and the 20C WRF simulations. Different storm tracking methods use different criteria and variables to detect and define features [e.g., see *Horn et al*., 2014]. To identify and follow coherent warm-cored cyclonic systems, we set minimum thresholds for the CZ02 detection criteria to be 30×10^{-5} s^{-1} of 850 hPa vorticity, a 0.51 K temperature anomaly, 15 m s^{-1} of 10 m wind speed, a minimum of 2 days of duration for the storm (nonconsecutive), and a tracking threshold for of 7×10^{-5} for the vorticity. For the H96 algorithm, the thresholds are 10×10^{-5} s^{-1} vertical vorticity detected as maxima in the 6 hourly relative vorticity field averaged over 850, 700, and 600 hPa levels, vorticity difference between levels at 200, 300, 400, 500, and 600 hPa for the warm-core test, 1000 mb of sea level pressure, and 17 m s^{-1} of 10 m wind speed.

Applying the CZ02 tracking schemes to the WRF regional climate simulations yielded a total of 182 TCs in the LGM over the 10 year simulation, 14 lower than tracked in 20C. (The annual average numbers of tropical

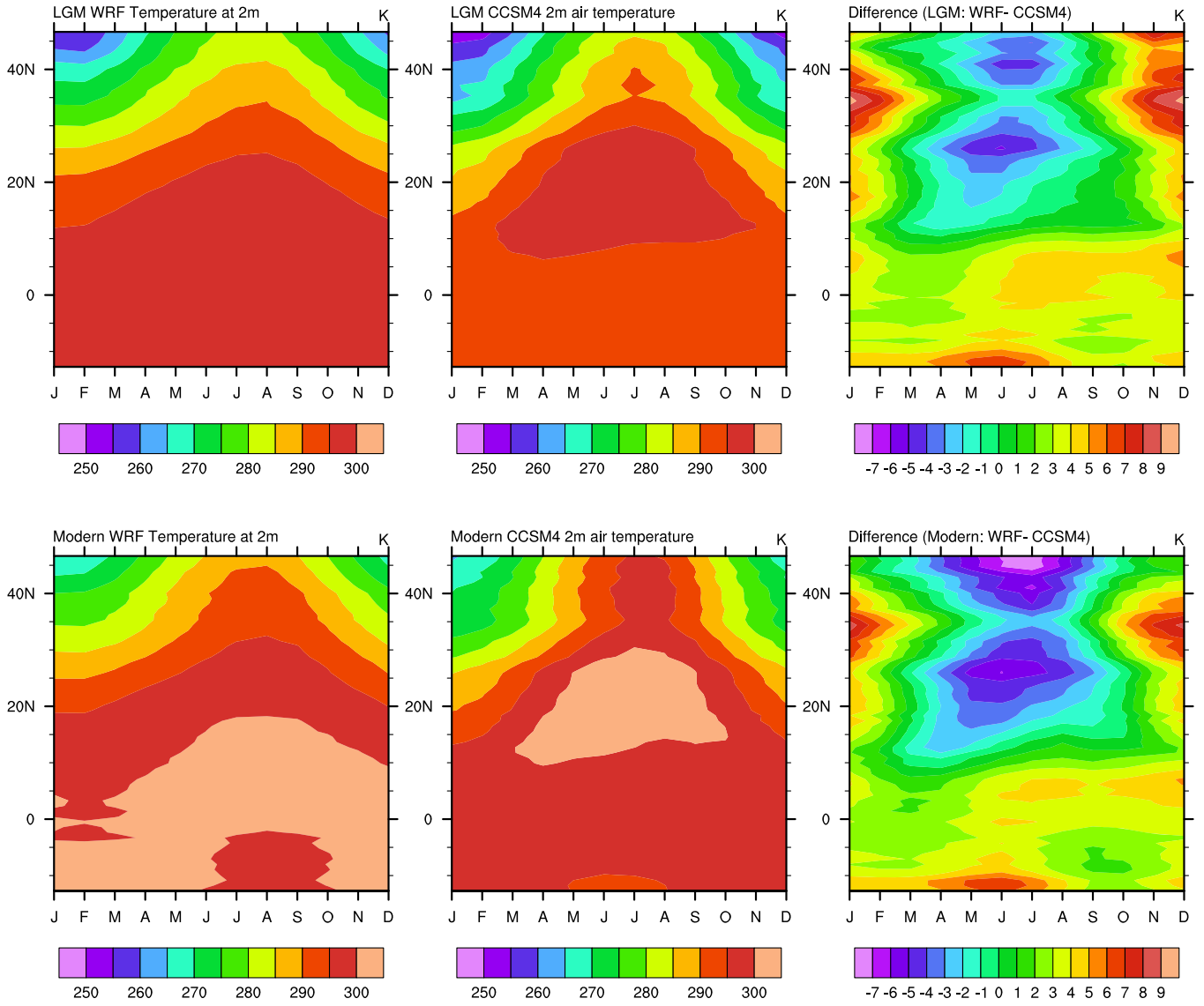

Figure 3. Ten year averages of the latitudinal and monthly distributions of 2 m air temperature (T2) from the WRF and CCSM4 simulations and their differences in both the (top) LGM and the (bottom) 20C.

cyclone (NTC) is 18.2 for LGM and 19.6 in 20C; see Table 2.) The H96 algorithm identified 201 TCs in the LGM, 27 more than in 20C. The median annual storm occurrence from CZ02 is 0.5 higher at LGM compared to 20C while the median is three higher at LGM in H96 (see box plot on left side of Figure 6). Given the small sample sizes and the large interannual variability, neither the differences in NTC between LGM and 20C using either CZ02 or H96 nor differences between these two algorithms within a single climate simulation are statistically significant (using a one-tailed t test with $p < 0.05$). Because the differences in storm counts between the two storm tracking schemes were not statistically significant, we proceed in the remainder of the study with an analysis of the results using the CZ02-generated track data set only. Despite the fact the differences are not statistically significant, it is noteworthy that the two algorithms yield different signs for the change in NTC between LGM and 20C; this highlights some of the variability inherent in different tracking algorithms, which can be especially large in their treatment of the weakest systems [*Horn et al.*, 2014].

Histograms in Figure 6 show the frequency distribution of the maximum wind speeds of each storm for the LGM and 20C (right top) and their probability density (right bottom). The storm intensity distributions are broadly similar during the LGM and 20C periods. While the 20C period produces stronger storms more frequently than during the LGM, the difference is not statistically significant. Figure 7 shows the annual cycles

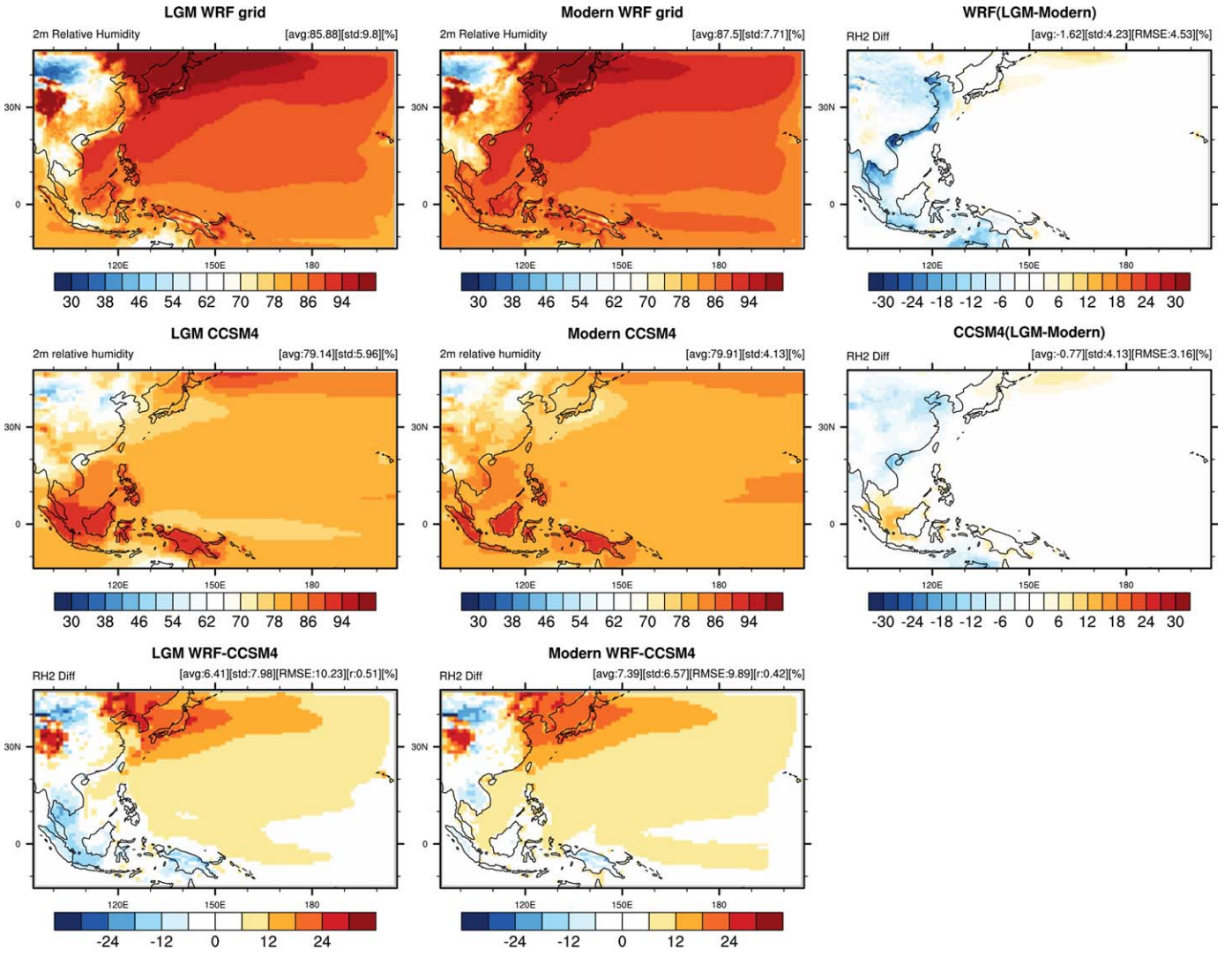

Figure 4. As in Figure 2 but for relative humidity at 2 m height.

of storm genesis number, accumulated cyclone energy (ACE), and power dissipation (PD) [*Emanuel*, 2005] for the LGM and 20C simulations. ACE and PD were computed by summing the square and cube of the maximum sustained surface winds every 6 h of each storm's lifespan, respectively.

The LGM annual cycle of events are similar to that of the 20C period, featuring a peak season from July to October. While storm frequency during the LGM is slightly lower than in the 20C period, ACE and PD is actually larger at LGM during August than in 20C.

To generate density plots, TC tracks were binned into 5° latitude by 5° longitude grid boxes for each period. Note that all the TCs were tracked only to 38°N to avoid any domain boundary effects on TC intensity [*Landman et al*., 2005]. Figure 8 shows TC genesis density and track density during the LGM and 20C periods, and the differences between the two. Both genesis density and track density difference plots (Figures 8e and 8f) show that LGM has a higher storm frequency in the corridor from 5°N, 160°E to the northwest toward Taiwan, while storm frequencies in the 20C period are higher over the South China Sea (e.g., near Hong Kong). Track density maps using the tracks computed from H96 show similar spatial distributions both for LGM and 20C (not shown). Differences of ACE and PD density between the LGM and 20C (Figure 9) suggest that TC activity in the LGM simulation was higher eastward of 150°E in the western North Pacific than in the 20C period, while TC activity is more frequent near the Asian coastal region in the 20C simulations.

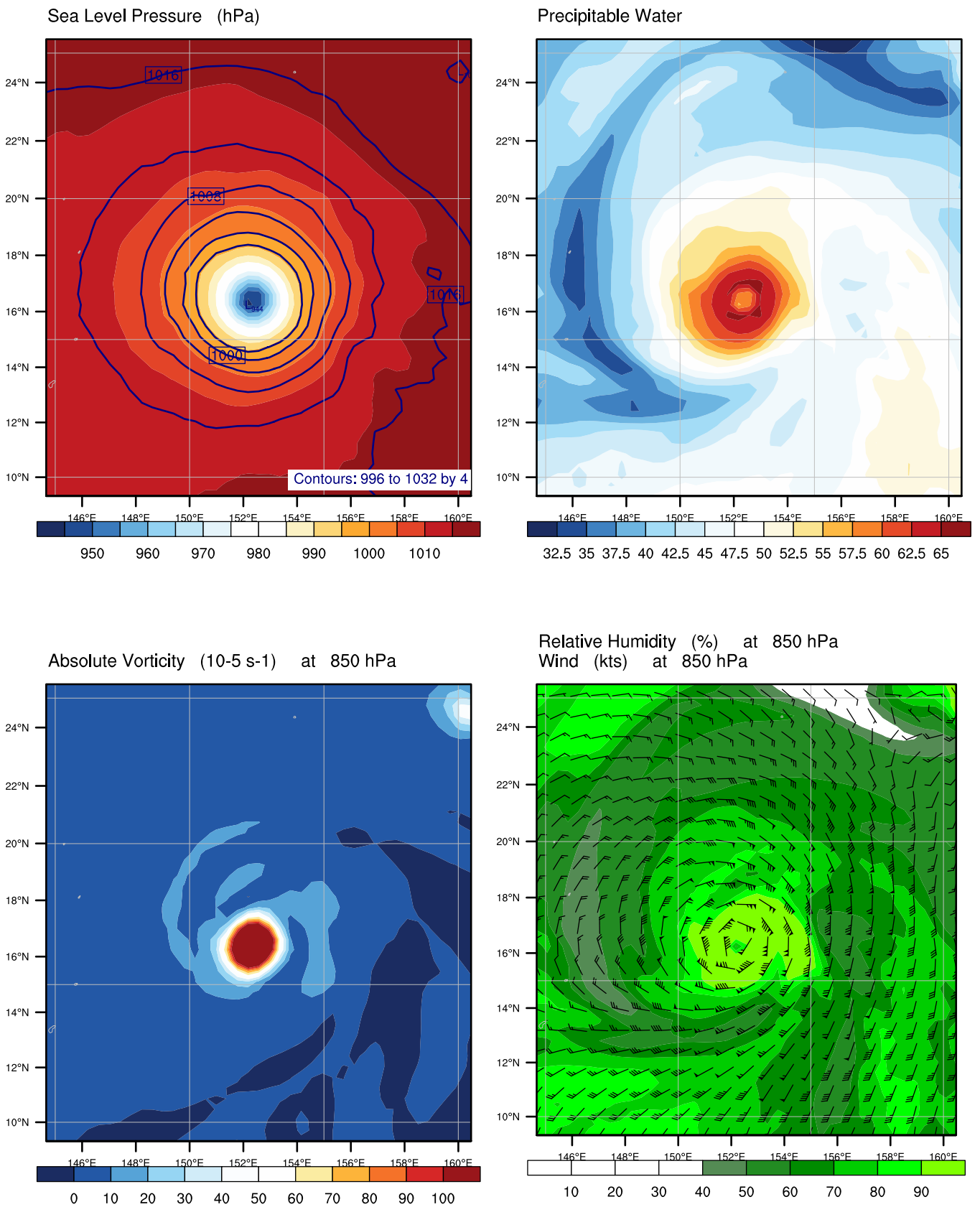

Figure 5. Enlarged images of an instantaneous WRF output during the LGM simulation for a typical tropical cyclone. (a) Sea level pressure (hPa), (b) precipitable water (mm), (c) 850 hPa absolute vorticity (10^{-5} s^{-1}), (d) relative humidity (%) and wind speed (kts) at 850 hPa.

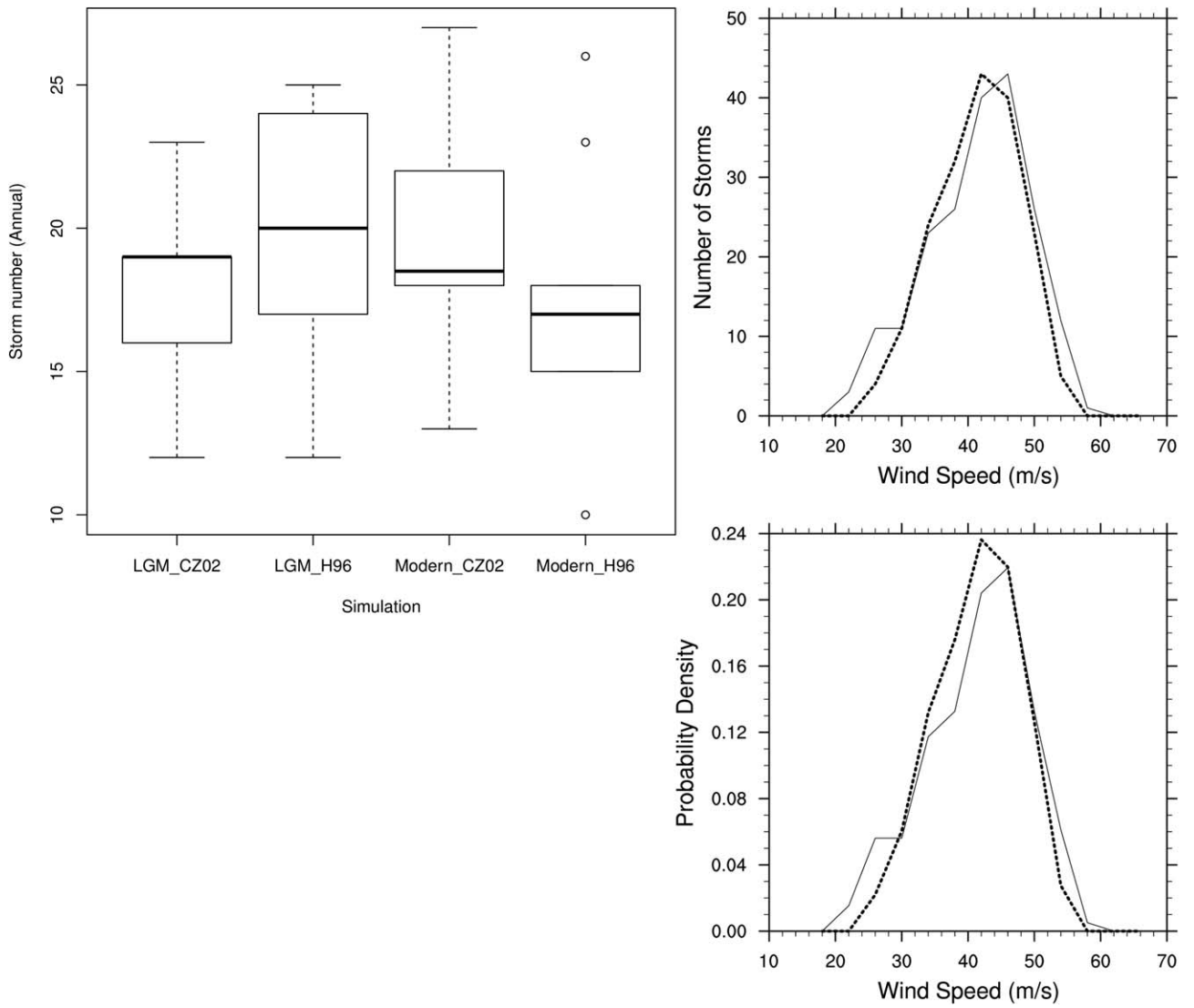

Figure 6. Box plot of TC occurrence from the LGM and 20C WRF simulations for the ten-year simulation period both from CZ02 (Left) and H96. The solid bars within each box indicates the median storm number, the bottom and top of the boxes indicate the first and third quartiles, and the whiskers indicate the minimum and maximum storm numbers. Open circles for Modern_H96 are outliers; and Histograms of maximum wind speeds (one value per storm; top right) and probability density (bottom right) for each western North Pacific storm simulated for the LGM (thick dot line) and 20C (thin line) periods.

Table 2. Frequency of Annual Tropical Cyclones and Their Statistics During the LGM and 20C Downscaling Simulations Using CZ02 and H96 Storm Tracking Schemes[a]

Simulation Year	CZ02-LGM	H96-LGM	CZ02-20C	H96-20C
1	19	16	19	23
2	19	25_M	27_M	15
3	19	17	13_μ	18
4	15	20	18	18
5	18	19	18	10_μ
6	19	24	18	18
7	22	20	22	16
8	23_M	23	17	15
9	12_μ	12_μ	19	15
10	16	25_M	25	26_M
Total	182	201	196	174
Average NTC	18.2	20.1	19.6	17.4
NTC Variance	9.36	16.49	14.84	18.04
Median annual count	19	20	18.5	17

[a]Largest (smallest) annual counts are marked with $_M(_\mu)$.

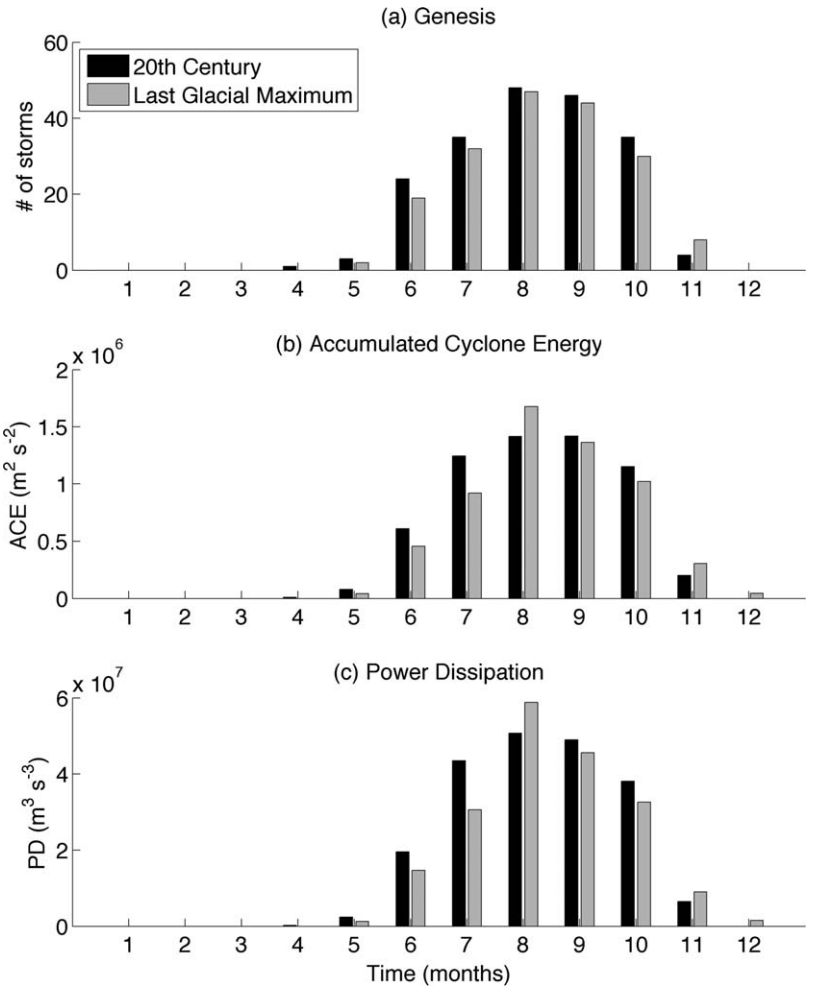

Figure 7. Annual cycles of storm genesis number, accumulated cyclone energy (ACE), and power dissipation (PD) by month.

5. Relationship to Large-Scale Environmental Conditions

We now consider how the climatology of downscaled TC activity is related to the large-scale environmental conditions that are most conducive for TC formation and intensification. *Korty et al*. [2012a] reviewed the development of contemporary genesis indices and discussed the physical reasons for choosing particular parameters. Briefly, TCs form in regions where surface fluxes from the ocean to the atmosphere raise the enthalpy of the atmospheric boundary layer and the thermal stability of the troposphere above supports deep moist convection. Regions where these conditions are met have high potential intensity (PI), which is a measure of how intense TCs can be based on the thermodynamic properties of the atmosphere [*Emanuel*, 1986, 1988; *Holland*, 1997; *Bister and Emanuel*, 2002]. High PI is generally found where both SST are high and tropospheric stability is low, conditions that were separately identified as important for genesis by *Gray* [1968] earlier. Regions where PI is low are coincident with those where the deep convection necessary to maintain intense tropical systems is untenable given the tropospheric sounding (see discussion in *Korty et al*. [2012b] for further detail). Strong vertical shear of the horizontal wind (hereafter, shear), defined here as the magnitude of the vector difference between the 200 and 850 hPa wind vectors, is detrimental to TCs [*Gray*, 1968; *DeMaria*, 1996]. In addition to the well-documented kinematic effects, shear also has a deleterious effect on the thermodynamic properties of the cyclone by entraining low-entropy, dry air from the environment into the saturated core of the system [*Tang and Emanuel*, 2010, 2012]. This highlights that higher levels of moisture in the middle troposphere are more favorable for genesis and intensification. In addition to reducing the magnitude of dry-air ventilation in the presence of shear, high midlevel moisture content also shortens the incubation period for nascent systems that must saturate the column during the genesis

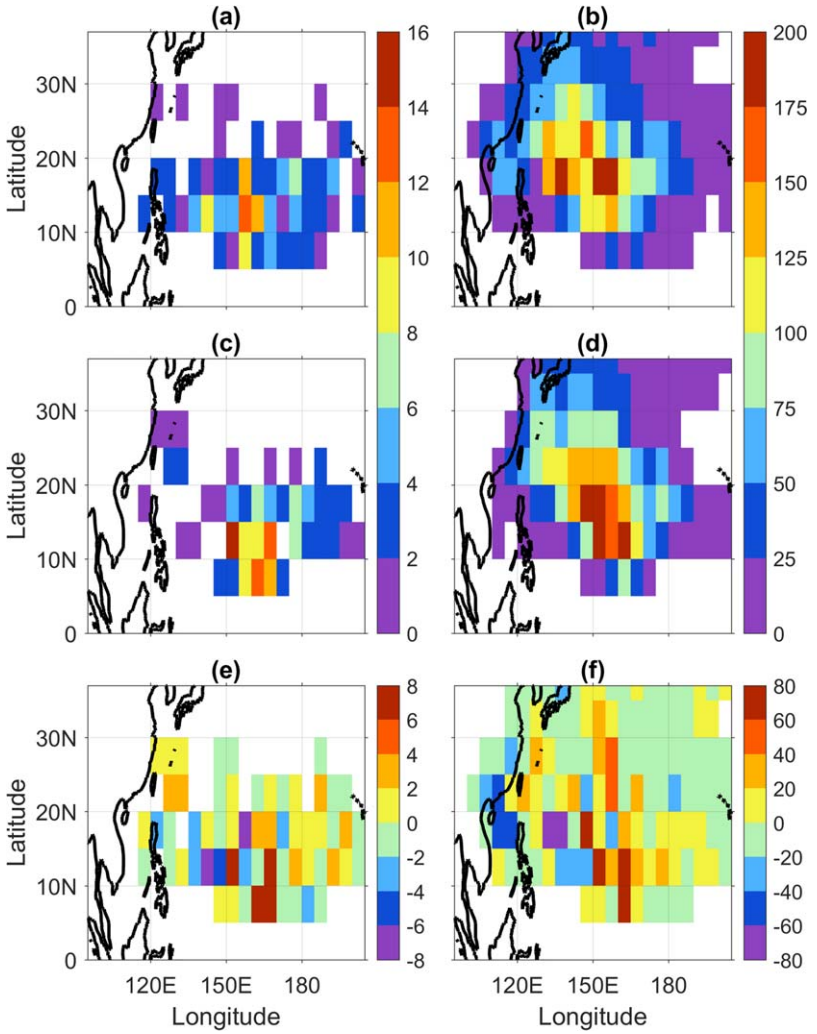

Figure 8. (left) Genesis density and (right) track density maps for the (top) 20C and (middle) LGM simulations, and (bottom) their differences between the LGM and 20C (LGM-20C).

process [*Rappin et al*., 2010]. Here we consider the relationship between each of these variables separately and in combination with the climatology of tracks in LGM and 20C presented in the last section.

5.1. Tropical Cyclone Potential Intensity

Average SSTs during the four most active months in the western North Pacific (July–October) are between 2°C and 3°C cooler at LGM than in 20C equatorward of 25°N (larger cooling is present poleward of this latitude). But as discussed by *Emanuel* [1987], there is no direct connection between any particular SST and potential intensity (PI). The implication of this, seen also in more recent work on TCs and contemporary climate change [e.g., *Vecchi and Soden*, 2007], is that the relationship between regions where TC formation is possible and the SSTs underlying them will vary with climate. Indeed, *Korty et al*. [2012a] showed that regions with vertical soundings capable of supporting the deep moist convection necessary to sustain TCs were coincident with areas where SSTs were warmer than 24°C in the LGM simulations (compared to ∼26°C in 20C).

PI values in 20C and LGM calculated in both CCSM4 and WRF are shown in Figure 10. Most importantly, despite the much colder temperatures, PI is less strongly changed through much of the western North Pacific. A second result of interest is that despite using the same temperatures to force CCSM4 and WRF, the values of PI in both 20C and at LGM are lower in WRF than in CCSM4. This in turn yields an important

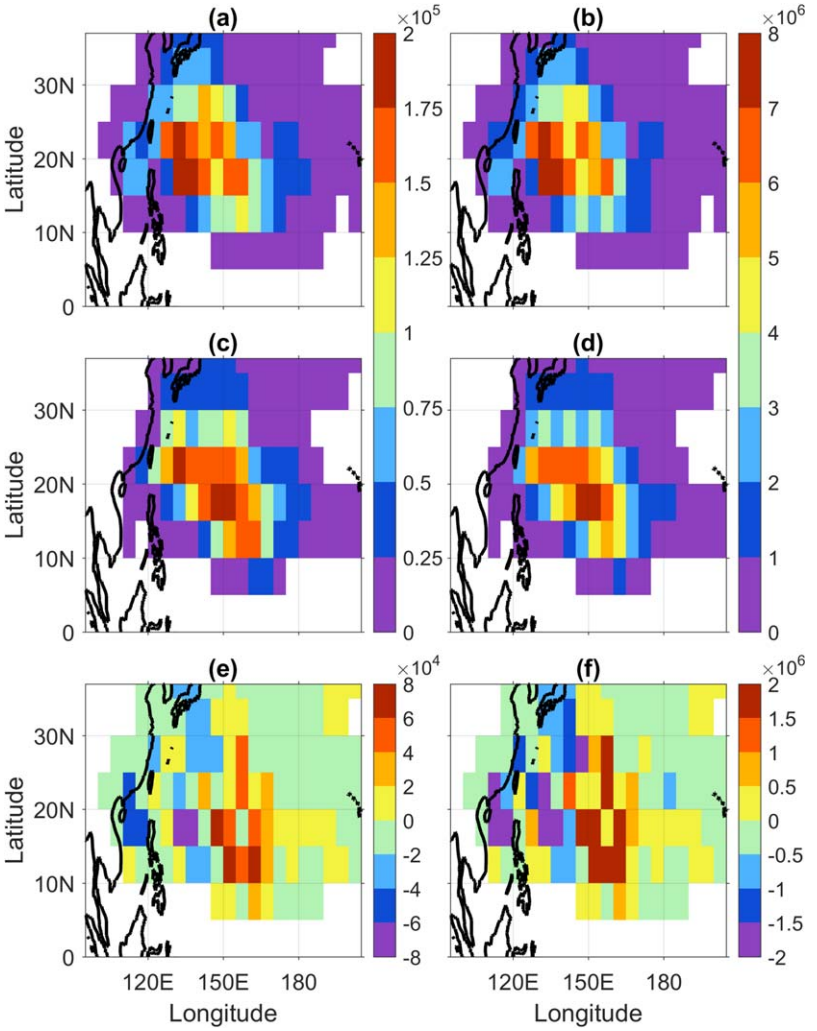

Figure 9. As in Figure 8 but for accumulated (left) cyclone energy (ACE) and (right) power dissipation (PD).

difference in the change in PI between LGM and 20C in the two models: it is slightly lower to little changed (relative to 20C) in much of the domain in CCSM4, but slightly higher in WRF.

These lower PI values at LGM in the WRF simulation are attributable to its higher boundary layer relative humidity (RH); near-surface values of RH over the western North Pacific are 0.8 in CCSM4, but are near 0.9 in WRF. *Emanuel* [1988] showed that the magnitude of the pressure drop possible in a TC increases proportionally with saturation deficit (i.e., 1-RH) in the boundary layer; that is, more intense storms are possible when the boundary layer begins further removed from saturation. The physical reason is that higher atmospheric boundary layer humidity levels reduce the strength of the air-sea enthalpy fluxes since the strength of evaporation is stronger in a drier boundary layer than in one near saturation. Given the nonlinearity of the PI calculation, the enthalpy fluxes decrease less with temperature for the more humid boundary layers (with smaller values of saturation deficit) in WRF than for the drier ones (with larger values of saturation deficit) in CCSM4. This correlation results in higher PI values at LGM in WRF through much of central part of the western North Pacific, even while the absolute values are lower in WRF than CCSM4.

The main result is that there is no significant change in the magnitude of PI in many parts of the western North Pacific in the WRF LGM simulation compared to WRF 20C simulation, but PI values are 2–4 m s^{-1} higher at LGM in the central part of the domain between 10°N and 20°N; this increase is statistically significant at the 95% confidence level (Figure 11). This region of higher PI values is qualitatively consistent with the region of higher LGM track density (Figure 8f), ACE density (Figure 9e) and PD density (Figure 9f) in the

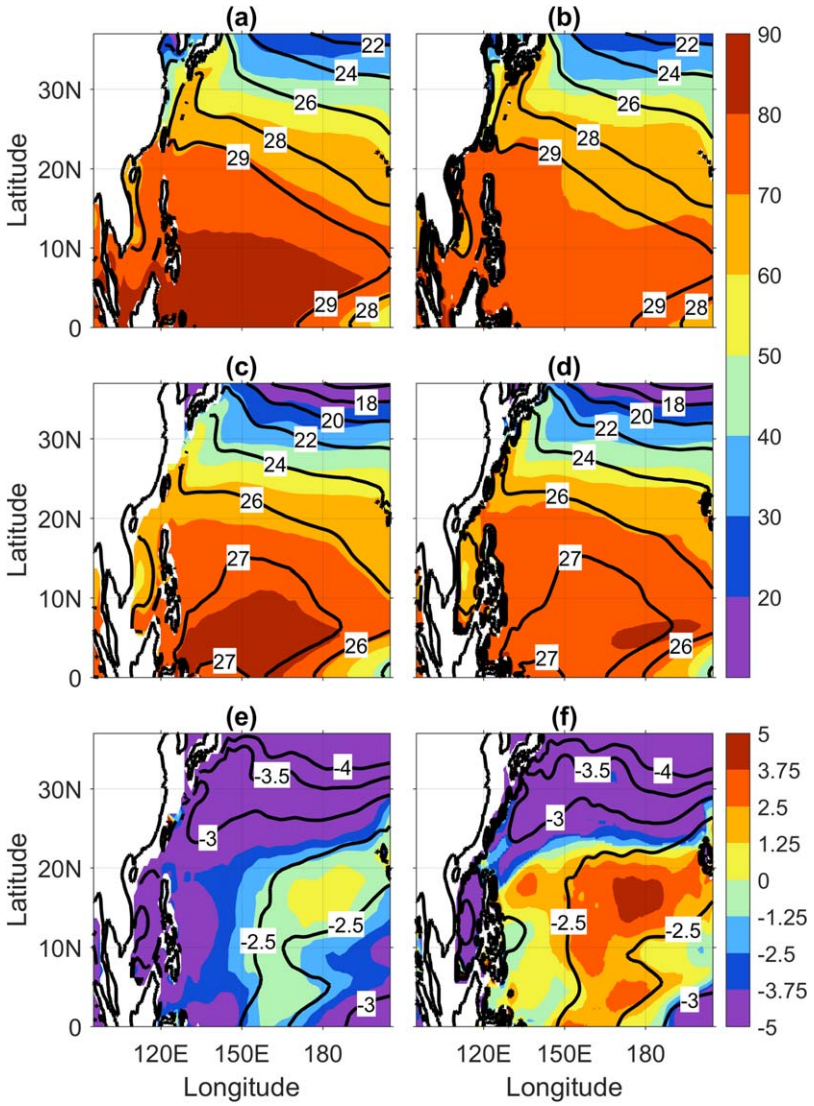

Figure 10. Storm season (JASO) maximum potential intensity (m s^{-1}) (color contour) superimposed by storm season mean sea surface temperature (black contour line) calculated from (left) CCSM4 and (right) WRF. PI for (top) the 20C control and (middle) the LGM and (bottom) PI difference plot between the two periods are shown.

region roughly bounded by 150°E, 180°E, 10°N, and 20°N. There are also decreases of PI at LGM over the South China Sea and in midlatitudes of the western North Pacific, that are statistically significant. Genesis and track densities are low in these areas in both climates (Figure 8), however.

5.2. Mid-Tropospheric Moisture Content

Tropospheric humidity is another important thermodynamic property for TC activity. *Emanuel* [1995] identified a nondimensional parameter that regulates the time needed for an incipient disturbance to saturate the middle troposphere to allow for intensification; larger values imply longer gestation. It is also a likely explanation for the decrease in storm frequency with warming observed in global climate models [e.g., *Emanuel et al*., 2008; *Camargo et al*., 2014]. The parameter is defined as:

$$\chi = \frac{s_m^* - s_m}{s_0^* - s_b} \tag{1}$$

where s_m^* is the saturation entropy in the middle troposphere (taken here using 600 mb data), s_m is the actual moist entropy of the middle troposphere (again using 600 mb data), s_0^* is the saturation entropy at the SST and surface pressure, and s_b is the actual moist entropy of the boundary layer (calculated using 925 mb

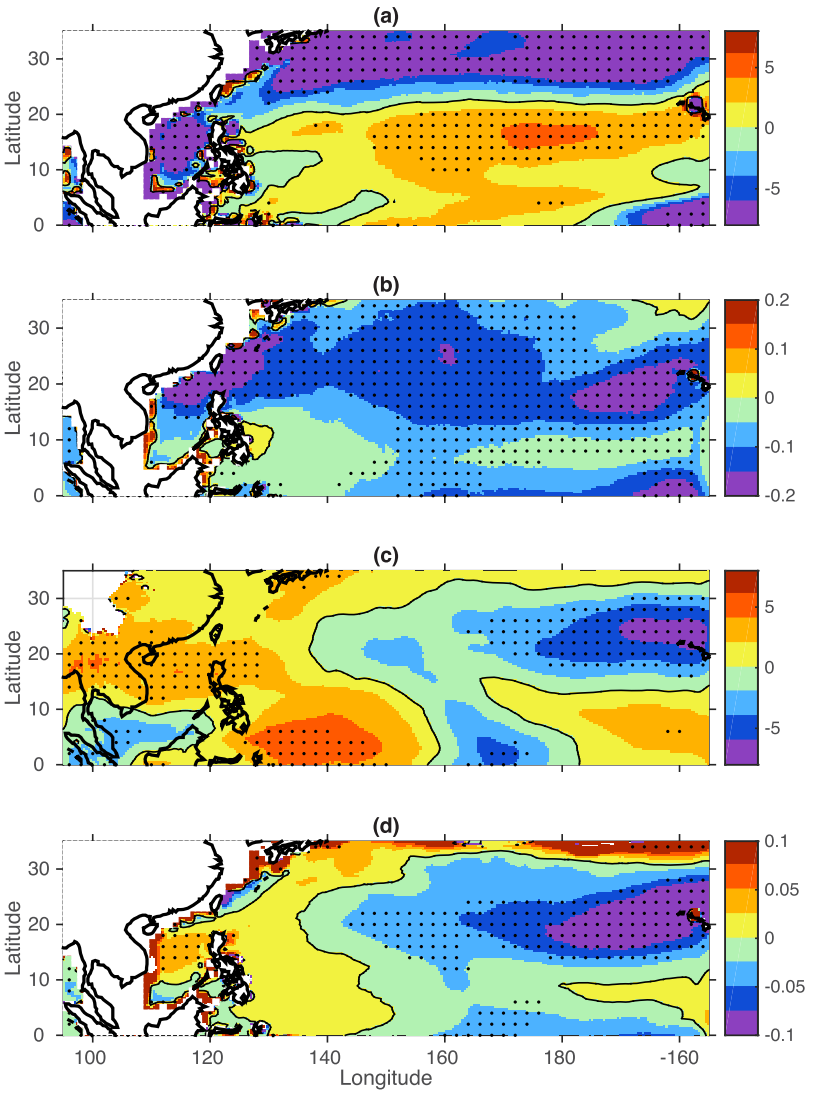

Figure 11. The *t* test results between the LGM and twentieth century WRF simulations for PI, Chi, shear, and lambda. Significant difference with 95% confidence level was stippled. Thick (dash) line represents zero (negative) contour values.

data here). This ratio gives a measure of the saturation deficit in the middle troposphere that must be eliminated by moist convective processes to the strength of the thermodynamic disequilibrium at the surface on which the fluxes fueling the convection depend. If RH remains constant, the numerator will decrease with temperature following the Clausius-Claperyon relation, while the denominator will decrease more slowly.

Figure 12 shows the spatial distribution of the saturation entropy deficit χ and relative humidity at 600 hPa for 20C, the LGM, and the difference between the two periods. As predicted, the lower temperatures at the LGM reduce the entropy deficit almost everywhere (Figure 12e), although the lower 600 hPa relative humidity (Figure 12f) somewhat offsets the decrease in χ one would otherwise expect with temperature. The changes in the entropy deficit over the western North Pacific between the LGM and 20C were statistically significant with 95% confidence level in general as shown in Figure 11. It is notable that mid-level relative humidity in the vicinity of the Philippines is lower at LGM than in 20C, which is consistent with the decrease of TC genesis and track density in the LGM simulation here (Figures 8e and 8f).

5.3. Wind Shear

Vertical wind shear has a deleterious effect on TC development and intensification in part by tilting the vortex [e.g., *Gray*, 1968; *DeMaria*, 1996; *Frank and Ritchie*, 2001]. Shear can prevent a storm from intensifying for thermodynamic reasons, as it mixes low-entropy dry air into the saturated convective core of the storm

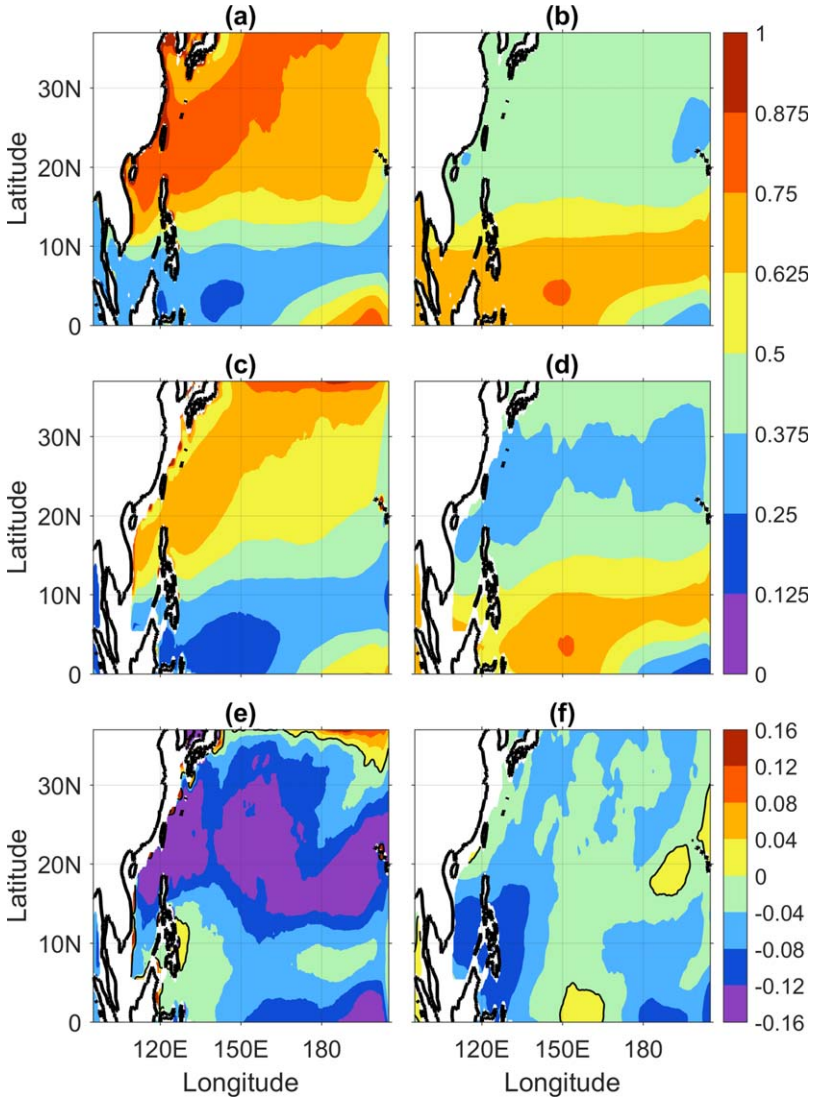

Figure 12. Storm season (JASO) (left) saturation entropy deficit (χ) and (right) 600 hPa relative humidity (%) for (top) the 20C control, (middle) the LGM, and (bottom) the difference between two periods (LGM-20C).

[*Rappin et al*., 2010; *Tang and Emanuel*, 2010, 2012]. *Nolan and Rappin* [2008] highlighted the complex role that even small values of vertical wind shear can exert in a changing climate: in the absence of any shear, the saturation of mid-troposphere can be reached quickly by increased surface fluxes in a warmer climate, but in the presence of even weak shear, the tendency to form more storms reversed with warming. *Nolan and Rappin* [2008] suggested that a warming climate might be unfavorable for TC genesis because unsaturated environmental air can desiccate the saturated core of a nascent storm by the mixing of the constant vertical shear, increasing the absolute saturation deficit in the mid-troposphere and decreasing the probability of TC genesis.

Figure 13 shows the storm season mean zonal wind shear (850–200 hPa) for the 20C (Figure 13a), LGM (Figure 13b), and the difference between the two periods (Figure 13c). The values shown here are the means of the vector difference of monthly mean 850 and 200 hPa wind vectors from all Julys to Octobers. Climatologically, the wind shear is lowest in between ~15°N and 25°N, with stronger shear in middle latitudes, east of the International Dateline, and southwest of the Philippines. The magnitude of the shear vector was greater at LGM through much of the western North Pacific basin, particularly nearer to the Asian continent, but it was little changed or lower in the central part of the domain eastward toward Hawaii (Figure 13c). Figure 11c shows that the changes in shear between the LGM and twentieth century are statistically

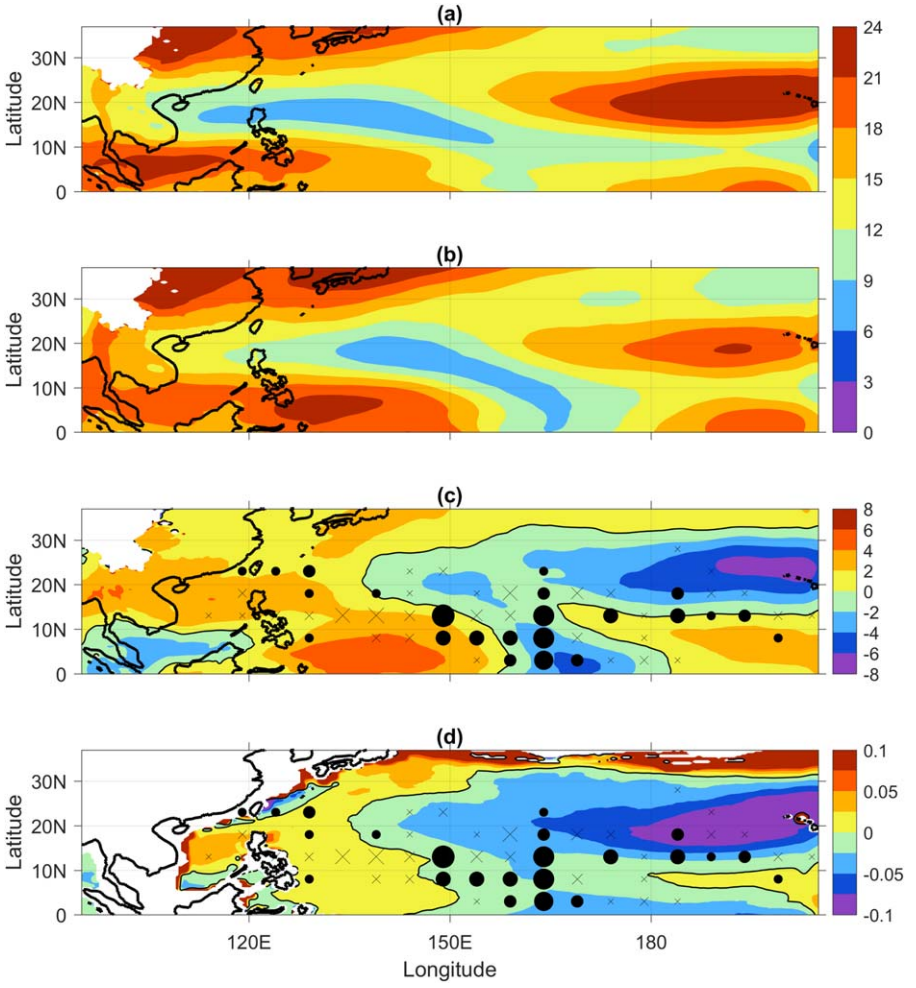

Figure 13. Magnitude of storm season (JASO) mean 200–850 hPa wind shear for (a) the 20C control, (b) the LGM, and (c) the difference between two periods (LGM-20C). (d) Difference in storm season mean ventilation index between two periods (LGM-20C). Cross (dot) marker symbols in (c) and (d) represent negative (positive) genesis density from difference between LGM and 20C simulations. Positive genesis density markers (dots) indicate higher favorability of TC genesis in the LGM over the 20C.

significant at the 95% confidence level in the western and eastern parts of the basin where the change is largest, but differences are not significant in the center part of the basin where mean values are ~1 m/s lower. This central region featured higher genesis density at LGM (Figure 13c) while genesis, ACE and PD densities are lower near the Philippines and in the South China Sea where wind shear was higher at LGM (see Figures 9e, 9f, and 13c).

5.4. Ventilation Index

The thermodynamic variables and wind shear examined earlier can each have an effect on TC genesis and activity, but in practice they do not operate in isolation. *Tang and Emanuel* [2012] showed that the effects of wind shear on storm development and intensification arise not only from kinematic effects through vortex tilting, but also through thermodynamic ones: stronger shears increase the rate of dry air intrusion from the surrounding environment, which in turn require increasingly large surface fluxes to maintain a supply of moisture sufficient to keep the column saturated. The cumulative effects were best measured by a nondimensional, normalized wind shear, or ventilation index, which *Tang and Emanuel* [2010] defined as:

$$\Lambda = \frac{V_{sh}\chi}{PI} \tag{2}$$

where V_{sh} is the magnitude of the 850–200 hPa wind shear vector, χ is defined as in equation (1), and PI is the potential intensity. Larger values of Λ, like larger values of wind shear, are detrimental to TCs.

Interestingly, *Tang and Camargo* [2014] showed that the ventilation index changes are consistent with changes in TC frequency in the CMIP5 models.

The differences in ventilation between the two climates and their statistical significance are shown in Figure 11d. These changes are qualitatively similar to pattern of changes in wind shear between the two climates (Figures 11c and 13c), though the area of lower ventilation index (more favorable conditions) at LGM covers a larger area through the central part of the western North Pacific than does more favorable wind shear alone. Importantly, the lower LGM ventilation values in the central part of the domain are statistically significant (Figure 11d) where the differences in shear were not (Figure 11c). The correspondence between regions of higher genesis density at LGM (black circles in Figures 13c and 13d) is aligned well with the more favorable ventilation index in the area, even though changes in the vertical wind shear are of mixed sign. The decreased ventilation index over the extratropical latitudes in the eastern part of the western North Pacific domain and the increased ventilation index over the South China Sea at the LGM are statistically significant changes from their values in 20C.

Spatial patterns of changes in the ventilation index (Figure 13d) of and genesis density (Figures 8e and 13d) suggest that the increase in TC genesis during the LGM occurred over the region where the combined effects of shear and thermodynamic variables yielded more favorable conditions than did the 20C period. In contrast, higher values of the vertical shear and ventilation index during the LGM over the South China Sea support the decreased TC genesis frequency near the Asian coastal region in the LGM (Figure 13d).

6. Summary and Conclusion

We simulated TCs in the LGM and late 20C in WRF on a 36 km grid by downscaling output from the global CCSM4 model. We found that the number of cyclones and their average intensity were not significantly different in the colder climate compared to modern times, which was broadly consistent with the spatial patterns of changes in environmental factors within this basin. Despite the much lower SSTs, potential intensity is locally higher at LGM in much of the central and eastern parts of the western North Pacific basin, where conditions cooled less than elsewhere in the tropics. Vertical wind shear and a measure of thermodynamic inhibition (c) were also lower here, and the density of tracks, ACE, and PD were larger. Near the coast of Asia, where conditions were less supportive for TCs at LGM than in modern times, densities of TCs were lower. The difference in the climatology of storms between the two climates aligned well with differences in the ventilation index measuring the combined effect of environmental changes.

Although there were no Category 4 and 5 TCs in our simulation, this higher spatial resolution offered by regional models compared to GCMs benefitted our understanding of cross-scale air-sea interactions and their influence on TC activities through the LGM and 20C downscaling simulations. In particular, the enhanced temporal and grid resolutions played a critical role in tracking and analyzing model-generated vortices, reducing the multiple sources of ambiguity in detecting storms existing in the GCM output.

Our results underscore the complexity of questions regarding how TCs respond to changes in climate. Despite the significantly colder global environment, conditions in this basin of this model were nevertheless locally more favorable for TCs than in the modern control case. Changes in the ventilation index—essentially a normalized measure of wind shear—predicted accurately the spatial structure of the changes in the distribution of downscaled storms. This relationship in these LGM simulations offer novel support for its ability to predict the changes to TC activity in other climates (both past and future) forced by changes to both wind shear and thermodynamic properties of the tropical atmosphere. While the results presented here came from only 10 years of downscaling driven by the output of a single climate model, the consistency between the WRF results and the large-scale environmental factors from CCSM4 and from previous studies give us confidence in our ability to simulate phenomena on the scale of TCs in paleoclimates and opens up exciting possibilities for applying regional climate models to questions raised by proxies in the geologic past.

Acknowledgments
We thank Dave Nolan and an anonymous reviewer for helpful comments on an earlier draft of this manuscript. This work was supported by the National Science Foundation through awards ATM-1064081, ATM-1064013, and ATM-1063837. All of the model code and data presented in this paper were obtained from the cited references.

References

Anthes, R. A. (1972), Development of asymmetries in a three-dimensional numerical model of the tropical cyclone, *Mon. Weather Rev.*, *100*, 461–476.

Bender, M. A., T. R. Knutson, R. E. Tuleya, J. J. Sirutis, G. A. Vecchi, S. T. Garner, and I. M. Held (2010), Modeled impact of anthropogenic warming on the frequency of intense Atlantic hurricanes, *Science*, *327*, 454–458.

Bister, M., and K. A. Emanuel (2002), Low frequency variability of tropical cyclone potential intensity: 1. Interannual to interdecadal variability, *J. Geophys. Res.*, *107*(D24), 4801, doi:10.1029/2001JD000776.
Braconnot, P., et al. (2007), Results of PMIP2 coupled simulations of the Mid-Holocene and Last Glacial Maximum—Part 1: Experiments and large-scale features, *Clim. Past*, *3*, 261–277.
Brady, E. C., B. L. Otto-Bliesner, J. E. Kay, and N. Rosenbloom (2013), Sensitivity to glacial forcing in the CCSM4, *J. Clim.*, *26*, 1901–1925.
Camargo, S. J. (2013), Global and regional aspects of tropical cyclone activity in the CMIP5 models, *J. Clim.*, *26*, 9880–9902, doi:10.1175/JCLI-D-12-00549.1.
Camargo, S. J., and A. A. Wing (2016), Tropical cyclones in climate models, *WIREs Clim. Change*, *7*, 211–237, doi:10.1002/wcc373.
Camargo, S. J., and S. E. Zebiak (2002), Improving the detection and tracking of tropical cyclones in atmospheric general circulation models, *Weather Forecasting*, *17*, 1152–1162.
Camargo, S. J., K. A. Emanuel, and A. H. Sobel (2007a), Use of a genesis potential index to diagnose ENSO effects on tropical cyclone genesis, *J. Clim.*, *20*, 4819–4834.
Camargo, S. J., A. H. Sobel, A. G. Barnston, and K. A. Emanuel (2007b), Tropical cyclone genesis potential index in climate models, *Tellus, Ser. A*, *59*, 428–443.
Camargo, S. J., M. K. Tippett, A. H. Sobel, G. A. Vecchi, and M. Zhao (2014), Testing the performance of tropical cyclone genesis indices in future climates using the HIRAM model, *J. Clim.*, *27*, 9171–9196.
Chan, J. C. L. (2015), Tropical cyclones in the western North Pacific, in *Encyclopedia of Atmospheric Sciences*, vol. 6, 2nd ed., pp. 77–84, Academic Press, Cambridge, Mass., doi:10.1016/B978-0-12-382225-3.00504-1.
CLIMAP Project Members (1976), The surface of the ice-age Earth, *Science*, *191*, 1131–1137.
Davis, C., et al. (2008), Prediction of landfalling hurricanes with the advanced hurricane WRF model, *Mon. Weather Rev.*, *136*, 1990–2005.
DeMaria, M. (1996), The effect of vertical shear on tropical cyclone intensity change, *J. Atmos. Sci.*, *53*, 2076–2087.
Done, J. M., L. R. Leung, and Y.-H. Kuo (2006), Understanding error in the long-term simulation of warm season rainfall using the WRF model, paper presented at 7th WRF Users Workshop, Nat. Cent. Atmos. Res., Boulder, Colo.
Done, J. M., G. J. Holland, C. L. Bruyere, L. R. Leung, and A. Suzuki-Parker (2015), Modeling high-impact weather and climate: Lessons from a tropical cyclone perspective, *Clim. Change*, *129*, 381–395.
Donnelly, J. P., and J. D. Woodruff (2007), Intense hurricane activity over the past 5000 years controlled by El Niño and the West African monsoon, *Nature*, *447*, 465–468.
Emanuel, K. A. (1986), An air–sea interaction theory for tropical cyclones. Part I: Steady-state maintenance, *J. Atmos. Sci.*, *43*, 585–605.
Emanuel, K. A. (1987), The dependence of hurricane intensity on climate, *Nature*, *326*, 483–485, doi:10.1038/326483a0.
Emanuel, K. A. (1988), The maximum intensity of hurricanes, *J. Atmos. Sci.*, *45*, 1143–1155.
Emanuel, K. A. (1995), The behavior of a simple hurricane model using a convective scheme based on subcloud-layer entropy equilibrium, *J. Atmos. Sci.*, *52*, 3959–3968.
Emanuel, K. A. (2005), Increasing destructiveness of tropical cyclones over the past 30 years, *Nature*, *436*, 686–688.
Emanuel, K. A. (2010), Tropical cyclone activity downscaled from NOAACIRES reanalysis, 1908-1958, *J. Adv. Model. Earth Syst.*, *2*, doi:10.3894/JAMES.2010.2.1.
Emanuel, K. A. (2013), Downscaling CMIP5 climate models shows increased tropical cyclone activity over the 21st century, *Proc. Natl. Acad. Sci. U. S. A.*, *110*, 12219–12224, doi:10.1073/pnas.1301293110.
Emanuel, K. A., R. Sundararajan, and J. Williams (2008), Hurricanes and global warming: Results from downscaling IPCC AR4 simulations, *Bull. Am. Meteorol. Soc.*, *89*, 347–367.
Emanuel, K. A., K. Oouchi, M. Satoh, T. Hirofumi, and Y. Yamada (2010), Comparison of explicitly simulated and downscaled tropical cyclone activity in a high-resolution global climate model, *J. Adv. Model. Earth Sys.*, *2*, 9, doi:10.3894/JAMES.2010.2.9.
Frank, W. M., and E. A. Ritchie (2001), Effects of vertical wind shear on the intensity and structure of numerically simulated hurricanes, *Mon. Weather Rev.*, *129*, 2249–2269.
Frappier, A., T. Knutson, K.-B. Liu, and K. Emanuel (2007), Perspective: Coordinating paleoclimate research on tropical cyclones with hurricane-climate theory and modelling, *Tellus, Ser. A*, *59*, 529–537.
Galewsky, J., C. P. Stark, S. J. Dadson, C.-C. Wu, A. H. Sobel, and M.-J. Horng (2006), Tropical cyclone triggering of sediment discharge in Taiwan, *J. Geophys. Res.*, *111*, F03014, doi:10.1029/2005JF000428.
Gray, W. M. (1968), Global view of the origin of tropical disturbances and storms, *Mon. Weather Rev.*, *96*, 669–700.
Hansen, J., A. Lacis, D. Rind, G. Russell, P. Stone, and I. Fung (1984), Climate sensitivity: Analysis of feedback mechanisms, in *Climate Processes and Climate Sensitivity, Geophys. Monogr. Ser.*, vol. *5*, pp. 130–163, AGU, Washington, D. C.
Hayakawa, Y. S., and O. Takashi (2009), GIS analysis of fluvial knickzone distribution in Japanese mountain watersheds, *Geomorphology*, *111*, 27–37.
Hobgood, J. S. (1986), A possible mechanism for the diurnal oscillations of tropical cyclones, *J. Atmos. Sci.*, *43*, 2901–2922.
Hobgood, J. S., and R. S. Cerveny (1988), Ice-age hurricanes and tropical storms, *Nature*, *333*, 243–245.
Hodges, K. I. (1994), A general method for tracking analysis and its application to meteorological data, *Mon. Weather Rev.*, *122*, 2573–2586.
Hodges, K. I. (1995), Feature tracking on the unit sphere, *Mon. Weather Rev.*, *123*, 3458–3465.
Hodges, K. I. (1996), Spherical nonparametric estimators applied to the UGAMP model intergration for AMIP, *Mon. Weather Rev.*, *124*, 2914–2932.
Holland, G. J. (1997), The maximum potential intensity of tropical cyclones, *J. Atmos. Sci.*, *54*, 2519–2541.
Horn, M., et al. (2014), Tracking scheme dependence of simulated tropical cyclone response to idealized climate simulations,. *J. Clim.*, *27*, 9197–9213, doi:10.1175/JCLI-D-14-00200.1.
Kieu, C. Q., and D.-L. Zhang (2008), Genesis of Tropical Storm Eugene (2005) from merging vortices associated with the ITCZ breakdowns. Part I: Observational and modeling analyses, *J. Atmos. Sci.*, *65*, 3419–3439.
Klotzbach, P. J., and C. W. Landsea (2015), Extremely intense hurricanes: Revisiting Webseter et al. (2005) after 10 years, *J. Clim.*, *28*, 7621–7629, doi:10.1175/JCLI-D-15-0188.1.
Knutson, T. R., J. J. Sirutis, S. T. Garner, G. A. Vecchi, and I. M. Held (2008), Simulated reduction in Atlantic hurricane frequency under twenty-first-century warming conditions, *Nat. Geosci.*, *1*, 359–364, doi:10.1038/ngeo202.
Knutson, T. R., J. L. McBride, J. Chan, K. Emanuel, G. Holland, C. Landsea, I. Held, J. P. Kossin, A. K. Srivastava, and M. Sugi (2010), Tropical cyclones and climate change, *Nat. Geosci.*, *3*, 157–163.
Knutson, T. R., J. J. Sirutis, M. Zhao, R. E. Tuleya, M. Bender, G. A. Vecchi, G. Villarini, and D. Chavas (2015), Global projections of intense tropical cyclone activity for the late twenty-first century from dynamical downscaling of CMIP5/RCP4.5 scenarios, *J. Clim.*, *28*, 7203–7224.

Koh, J. H., and C. M. Brierley (2015), Tropical cyclone genesis potential across palaeoclimates, *Clim. Past*, *11*, 1433–1451, doi:10.5194/cp-11-1433-2015.
Korty, R. L., S. J. Camargo, and J. Galewsky (2012a), Tropical cyclone genesis factors in simulations of the Last Glacial Maximum, *J. Clim.*, *25*, 4348–4365.
Korty, R. L., S. J. Camargo, and J. Galewsky (2012b), Variations in tropical cyclone genesis factors in simulations of the Holocene epoch, *J. Clim.*, *25*, 8196–8211.
Kumar, A., J. M. Done, J. Dudhia, and D. Niyogi (2011), Simulations of cyclone Sidr in the Bay of Bengal with a highresolution model: Sensitivity to large-scale boundary forcing, *Meteorol. Atmos. Phys.*, *114*, 123–137, doi:10.1007/s00703-011-0161-9.
Landman, W. A., A. Seth, and S. J. Camargo (2005), The effect of regional climate model domain choice on the simulation of tropical cyclone-like vortices in the Southwestern Indian Ocean, *J. Clim.*, *18*, 1263–1274.
Landsea, C. W., B. A. Harper, K. Hoarau, and J. A. Knaff (2006), Can we detect trends in extreme tropical cyclones?, *Science*, *313*, 452–454, doi:10.1126/science.1128448.
Lin, G. W., H. Chen, N. Hovius, M. J. Horng, S. Dadson, P. Meunier, and M. Lines (2008), Effects of earthquake and cyclone sequencing on landsliding and fluvial sediment transfer in a mountain catchment, *Earth Surf. Processes Landforms*, *33*, 1354–1373.
Liu, K.-B., and M. L. Fearn (1993), Lake-sediment record of late Holocene hurricane actvities from coastal Alabama, *Geology*, *21*, 793–796.
Lo, J. C.-F., Z.-L. Yang, and R. A. Pielke Sr. (2008), Assessment of three dynamical climate downscaling methods using the Weather Research and Forecasting (WRF) model, *J. Geophys. Res.*, *113*, D09112, doi:10.1029/2007JD009216.
Merlis, T. M., W. Zhou, I. M. Held, and M. Zhao (2016), Surface temperature dependence of tropical cyclone-permitting simulations in a spherical model with uniform thermal forcing, *Geophys. Res. Lett.*, *43*, 2859–2865, doi:10.1002/2016GL067730.
Murakami, H., et al. (2012), Future changes in tropical cyclone activity projected by the new high-resolution MRI-AGCM, *J. Clim.*, *25*, 3237–3260.
Murakami, H., et al. (2015), Simulation and prediction of category 4 and 5 hurricanes in the high-resolution GFDL HiFLOR coupled climate model, *J. Clim.*, *28*, 9058–9079, doi:10.1175/JCLI-D-15-0216.1.
Nolan, D. S., and E. D. Rappin (2008), Increased sensitivity of tropical cyclogenesis to wind shear in higher SST environments, *Geophys. Res. Lett.*, *35*, L14805, doi:10.1029/2008GL03414.
Rappin, E. D., D. S. Nolan, and K. A. Emanuel (2010), Thermodynamic control of tropical cyclogenesis in environments of radiative-convective equilibrium with shear, *Q. J. R. Meteorol. Soc.*, *136*, 1954–1971.
Skamarock, W. C., J. B. Klemp, L. Dudhia, D. O. Gill, D. M. Barker, W. Wang, and J. G. Powers (2005), A description of the advanced research WRF Version 2, *NCAR Tech. Note TN-468+STR*, 88 pp., Natl. Cent. for Atmos. Res., Boulder, Colo.
Stark, C. P., J. R. Barbour, Y. S. Hayakawa, T. Hattanji, N. Hovius, H. Chen, C.-W. Lin, M.-J. Horng, K.-Q. Xu, and Y. Fukahata (2010), The climatic signature of incised river meanders, *Science*, *327*, 1497–1501, doi:10.1126/science.1184406.
Sugi, M., K. Yoshida, and H. Murakami (2015), More tropical cyclones in a cooler climate?, *Geophys. Res. Lett.*, *42*, 6780–6784, doi:10.1002/2015GL064929.
Tang, B., and S. J. Camargo (2014), Environmental control of tropical cyclones in CMIP5: A ventilation perspective, *J. Adv. Model. Earth Syst.*, *6*, 115–128, doi:10.1002/2013MS000294.
Tang, B., and K. A. Emanuel (2010), Midlevel ventilation's constraint on tropical cyclone intensity, *J. Atmos. Sci.*, *67*, 1817–1830.
Tang, B., and K. A. Emanuel (2012), A ventilation index for tropical cyclones, *Bull. Am. Meteor. Soc.*, *93*, 1901–1912.
Toomey, M. R., W. B. Curry, J. P. Donnelly, and P. J. van Hengstum (2013), Reconstructing 7000 years of North Atlantic hurricane variability using deep-sea sediment cores from the western Great Bahama Bank, *Paleoceanography*, *28*, 31–41.
Vannitsem, S., and F. Chome (2005), One-way nested regional climate simulations and domain size, *J. Clim.*, *18*, 229–233.
Vecchi, G. A., and B. J. Soden (2007), Effect of remote sea surface temperature change on tropical cyclone potential intensity, *Nature*, *450*, 1066–1070.
Walsh, K. *J. E.*, et al. (2016), Tropical cyclones and climate change, *WIREs. Clim. Change*, *7*, 65-89.
Webster, P. J., G. J. Holland, J. A. Curry, and H.-R. Chang (2005), Changes in tropical cyclone number, duration, and intensity in a warming environment, *Science*, *309*, 1844–1846, doi:10.1126/science.1116448.
Woodruff, J. D., J. P. Donnelly, and A. Okusu (2009), Exploring typhoon variability over the mid-to-late Holocene: Evidence of extreme coastal flooding from Kamikoshiki, Japan, *Quat. Sci. Rev.*, *28*, 1774–1785.
Yu, E., T. Wang, Y. Gao, and W. Xiang (2014), Precipitation pattern of the mid-Holocene simulated by a high-resolution regional climate model, *Adv. Atmos. Sci.*, *31*, 962–971, doi:10.1007/s00376-013-3178-9.
Zhao, M., and I. M. Held (2012), TC-permitting GCM simulations of hurricane frequency response to sea surface temperature anomalies projected for the late-twenty-first century, *J. Clim.*, *25*, 2995–3009.